Nanoscale

PAPER

View Article Online
View Journal | View Issue

Check for updates

Cite this: *Nanoscale*, 2024, **16**, 11604

Enhancing the electronic structure of Ni-based electrocatalysts through N element substitution for the hydrogen evolution reaction†

Yibin Yang,[a] Xin Jin,[b] Fangyang Zhan*[c] and Yang Yang*[d]

Received 13th March 2024,
Accepted 22nd May 2024

DOI: 10.1039/d4nr01071j

rsc.li/nanoscale

The weak orbital coupling between Ni_3N and H_2O, caused by its interstitial structure and attenuated Ni–N interaction, is attributed to the high unoccupied d orbital energy of Ni_3N. Consequently, the kinetics for water dissociation in the HER are slow. In this study, we effectively lowered the energy state of vacant d orbitals in Ni_3N, which resulted in an exceptionally efficient HER. The as-synthesized Ni_3N catalyst demonstrates an overpotential of 135 mV when subjected to a current density of 10 mA cm^{-2}. The refined structural characterization suggests that the introduction of oxygen results in a reduction in electron densities surrounding the Ni sites. Furthermore, DFT calculations provide additional evidence that the electrocatalyst of Ni_3N generates a greater number of lowest unoccupied orbitals (LUMOs) and improved alignment, thereby enhancing the adsorption and splitting of water. The notion of orbital-regulated electronic levels on Ni sites introduces a distinctive methodology for the systematic development of catalysts used in hydrogen evolution and other applications.

Published on 03 1403. Downloaded on 28/11/1404 09:10:16 ..

Introduction

In recent years, the electrochemical hydrolysis method has gained increasing attention owing to its high efficiency and environmentally friendly nature, making it a promising approach for generating high-purity hydrogen, and electrocatalytic water splitting undoubtedly has the potential to decelerate the consumption of conventional fossil fuels and alleviate the burden of environmental pollution.[1–4] However, the hydrogen evolution reaction (HER) requires a high overpotential,[1,5–9] which inevitably limits the application of hydrogen production in industrial practice. Currently, Pt-based electrocatalysts are widely recognized as active electrocatalysts for the HER because of their optimal Pt–H bond strength and Gibbs free energy (ΔG) to form the Pt–H bond.[10–13] However, the widespread application of these resources is impeded by their exorbitant cost. Therefore, the development of platinum-free electrocatalysts, which are both cost-effective and exhibit superior HER performance, is of paramount importance. This is a critical step towards realizing large-scale hydrogen production.[14–18]

Over the past several years, significant progress has been accomplished in the quest for cost-effective and efficient electrocatalysts for the HER.[9,19–22] This success is attributed to the relentless efforts and comprehensive research conducted in this field. Transition metal oxides,[23–26] sulfides[15,19,27] and carbides[28–32] have been developed and widely used as alternatives to precious metal electrocatalysts for the HER in acid and/or alkaline solutions. However, the major drawback of these electrocatalysts lies in their inadequate electron conductivity, which significantly impedes the transport of electrons from the surface of the electrocatalyst to the supporting electrode. Furthermore, the inadequate electron conductivity occasionally results in the formation of Schottky barriers at both the electrocatalyst-electrolyte and the electrocatalyst-support electrode interface. Consequently, additional overpotential is required to overcome these energy barriers, resulting in a decrease in energy conversion efficiency. Hence, researchers have identified two effective approaches for designing active catalysts within these systems. The initial approach involves the incorporation of additional active sites for the HER and the induction of structural disorders. Numerous studies have been dedicated to enhancing the density of electrocatalytic active sites *via* forming defects. The second

[a]*Chemical Pollution Control Chongqing Applied Technology Extension Center of Higher Vocational Colleges, Chongqing Industry Polytechnic College, Chongqing 401120, PR China*
[b]*College of Physics and Electronic Engineering, Chongqing Normal University, Chongqing 401331, P. R. China*
[c]*Institute for Structure and Function & Department of Physics, Chongqing University, Chongqing 400044, P. R. China. E-mail: zhan_fyang@cqu.edu.cn*
[d]*Key Laboratory of Chemical Additives for China National Light Industry, College of Chemistry and Chemical Engineering, Shaanxi University of Science & Technology, 710021 Xi'an, China. E-mail: yyang399@sust.edu.cn*

† Electronic supplementary information (ESI) available. See DOI: https://doi.org/10.1039/d4nr01071j

This journal is © The Royal Society of Chemistry 2024

Published on 03 1403. Downloaded on 28/11/1404 09:10:16 ..

approach focuses on improving the electrical conductivity of electrocatalysts. Considerable research has been conducted to investigate the utilization of conducting materials as catalyst supports in order to improve the electrical conductivity of the electrocatalysts. With the aforementioned problems of electrocatalysts, significant efforts are dedicated to enhancing the performance of the HER by improving both of these factors.

Recently, transition metal nitrides (TMNs) have emerged as highly efficient electrocatalysts for hydrogen production.[18,28,33–41] This is primarily due to their metallic nature, which enables enhanced electrocatalytic activity. The remarkable catalytic performance of these TMNs within the HER domain can be ascribed to their distinctive electronic configuration. This unique structure promotes optimal proton adsorption onto the nitride surface throughout the electrocatalytic reaction. The incorporation of catalysts with high metallicity significantly enhances electron transport in the HER process, thereby promoting the overall activity of HER. Recently, Zhang *et al.*[34] have successfully developed a 3D porous nickel molybdenum nitride material that demonstrates exceptional performance in HER. Additionally, they presented an efficient water electrolysis device, which is based on hierarchical TiN@Ni_3N nanowire arrays.[34] Theoretical investigations suggest that Ni_3N possesses intrinsic metallic properties and has excellent electrical conductivity.[36] In addition, the disordered atomic structure of nanosheets that are only a few atoms thick can offer a greater number of active sites. Accordingly, it is anticipated that 2D Ni_3N nanosheets will exhibit exceptional electrocatalytic activity. Specifically, uncovering the exact active site location of Ni_3N is expected to serve as an effective protocol for enhancing the activity of HER and designing electrocatalysts for HER. Among many materials, Ni_3N is enormously favored by researchers because of its excellent conductivity. However, the water dissociation efficiency of Ni_3N is insufficient, while the energy barrier for HER is prohibitively elevated. The markedly inferior performance of Ni_3N in comparison to Pt can be attributed to primary factors, thereby presenting substantial opportunities for enhancement. The coupling effect of the interface is instrumental in augmenting the electrocatalytic activity. This enhancement is achieved through the regulation of the local electronic structure at the interface, which in turn adjusts the orbital overlap among various atoms. Ultimately, this process modifies the strength of adsorption–desorption between the electrocatalysts and the reaction intermediates. Therefore, integrating an appropriate element into Ni_3N to establish a composite, characterized by a robust interface coupling effect, harbors significant potential for augmenting the electrocatalytic activity.

In this study, we present the design and synthesis of 3D Ni_3N/NF to improve the performance of HER in 1.0 M KOH. Benefiting from the robust chemical coupling and synergistic effects at the interface of the electrocatalysts, the Ni_3N/NF hybrid electrode demonstrates exceptional catalytic performance for HER. The single NiO electrode is surpassed by achieving an overpotential of a mere 135 mV at a current density of 10 mA cm^{-2} in a 1 M KOH solution, demonstrating a reduction of 177 mV. Moreover, the utilization of 3D metallic Ni_3N nanosheets can lead to further enhancements in carrier concentration and electrical conductivity, as demonstrated by DFT calculations. Specifically, the Ni site on the Ni_3N surface exhibits the lowest ΔG_{H^*} value of 1.63 eV. This can be attributed to the coupling effect between the Ni site and N atoms around the Ni site, making these sites the most active for the HER in Ni_3N. The Ni_3N nanosheets we have developed and studied, which exhibit excellent hydrogen evolution reaction activity under the guidance of a supervisor, hold significant potential for future applications in hydrogen production technologies.

Results and discussion

The $Ni(OH)_2$/NF nanosheets array, shown in Fig. 1a, was directly grown on Ni foam using a hydrothermal method. Subsequently, the $Ni(OH)_2$/NF was calcined under NH_3 atmosphere at 400 °C to obtain Ni_3N/NF. Fig. 1b illustrates the XRD patterns of the as-synthesized $Ni(OH)_2$, NiO, and Ni_3N nanosheets scraped down from NF. The XRD patterns of Ni_3N/NF (JCPDS Card No. 10-0280) are represented by the green line in Fig. 1b. The diffraction peaks observed, specifically (110), (002), (112), (300), (111), (200), (220), and (113), exhibit a sequence of Bragg reflections. These reflections align harmoniously with the established patterns of Ni_3N and nickel foam, thereby confirming their consistency. The diffraction peaks identified at 44.4°, 51.8°, and 76.3° correspond respectively to the (111), (200), and (220) planes of the nickel foam (Ni, JCPDS Card No. 01-1258). Therefore, the successful synthesis of Ni_3N/NF is confirmed. Additionally, NiO/NF (violet line) and $Ni(OH)_2$/NF (blue line) were also successfully prepared. Fig. 1c demonstrates the scanning electron microscopy (SEM) image

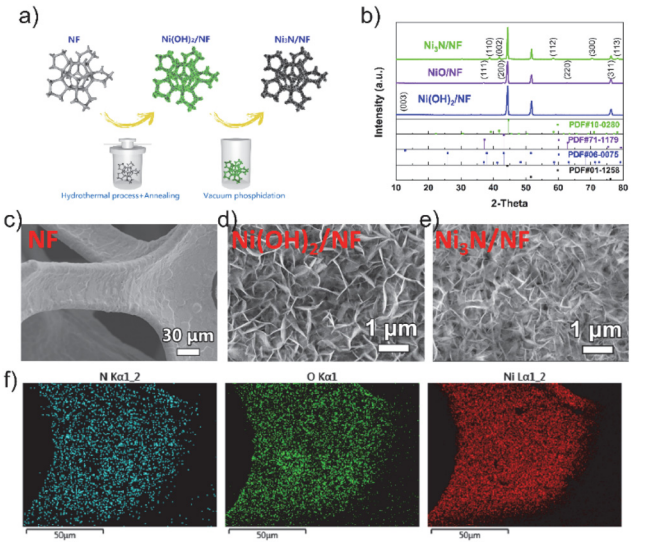

Fig. 1 (a) A schematic of the synthesis process of Ni_3N; (b) XRD patterns of as-prepared $Ni(OH)_2$/NF, NiO/NF and Ni_3N/NF; (c) SEM image of nickel foam; (d and e) SEM images of as-prepared $Ni(OH)_2$/NF, NiO/NF and Ni_3N/NF nanosheets; (f) EDX patterns of Ni_3N/NF.

Published on 03 1403. Downloaded on 28/11/1404 09:10:16 ..

of the three-dimensional open porous structure of the NF. The SEM images in Fig. 1d and e show the vertical growth of nanosheets of $Ni(OH)_2$ and Ni_3N on the NF substrate, respectively. The nanosheet morphology is further revealed in the transmission electron microscopy (TEM) image shown in Fig. S1.† The formation of the crystallized phase of Ni_3N is confirmed in Fig. S2.† Additionally, the high-resolution transmission electron microscopy (HRTEM) image presented in Fig. S3† exhibits distinct lattice fringes with an interplanar spacing of 0.24 nm, which is indicative of the (110) plane of the nickel nitride (Ni_3N) nanosheets. Furthermore, the selected area electron diffraction (SAED) patterns, as illustrated in Fig. S4,† reveal diffraction rings that are indicative of the (001) and (110) planes of the Ni_3N nanosheets. These observations are in agreement with the X-ray diffraction (XRD) patterns, specifically the green line in Fig. 1b, confirming the crystallographic planes of the Ni_3N nanosheets. In order to ascertain the spatial distribution of individual elements within the nickel foam, energy dispersive X-ray spectroscopy (EDS) elemental mapping analysis was conducted. Fig. 1f clearly illustrates a homogeneous distribution of Ni and N elements, with no discernible segregation. This suggests the successful synthesis of Ni_3N on the NF substrate. However, the presence of oxygen in the samples is indicated by EDS (Fig. 1f), which could be attributed to oxide or absorbed oxygen species.

X-ray photoelectron spectroscopy (XPS) was utilized to examine the influence of non-metallic elements on the surface conditions and electronic configuration of the freshly synthesized NiO, Ni_3N, and $Ni(OH)_2$ specimens. The XPS survey spectra, as depicted in Fig. 2a, indicate that the samples display analogous survey spectra. However, an exception is noted in the form of a minor peak, which is ascribed to the existence of the N element in the Ni_3N sample. The high-resolution Ni 2p spectra of $Ni(OH)_2$, as depicted in Fig. 2b, exhibit two peaks. These peaks, with binding energies at 855.8 eV and 873.7 eV, correspond to the Ni^{2+} $2p_{3/2}$ and Ni^{2+} $2p_{1/2}$ states, respectively. This observation aligns with findings from a prior study.[42] Compared with $Ni(OH)_2$, the peak positions of NiO (855.9 eV and 853.6 eV) and Ni_3N (854.9 eV and 852.9 eV) in the electrocatalysts are shifted to lower energies, elucidating that O and N in the electrocatalysts figure electron-rich centres and the Ni atoms in the NiO and Ni_3N receive electron transfers from O and Ni, respectively. Especially, the peak position of Ni atoms in Ni_3N is lower than that of the Ni atoms in NiO and $Ni(OH)_2$, indicating the Ni atoms in Ni_3N receive more electrons than the Ni atoms in NiO and $Ni(OH)_2$. Additionally, the XPS O 1s profiles in $Ni(OH)_2$ can typically be deconvoluted into two dominating characteristic peaks at 533.6 eV and 532.1 eV, which corresponded to the absorbed O species, *e.g.*, water molecules and surface hydroxyl groups, respectively (Fig. 2c). In comparison with the peak position of O atoms in $Ni(OH)_2$, the peak position of the O atoms in NiO (533.1 eV and 530.8 eV) peaks also exhibits an obvious negative shift, suggesting that the O atoms in NiO receive more electrons than the O atoms in $Ni(OH)_2$. The high-resolution N 1s spectrum of Ni_3N exhibits a peak at 398.2 eV, which corresponds to the bound N element (Fig. 2d). In comparison with the XPS peak of N 1s in N_2 at 406 eV,[43] the electron is transferred from the N atom to the Ni atom in Ni_3N. In other words, the charge is transferred from N-sites to Ni-sites in Ni_3N, and the number of electrons on the Ni-site in the electrocatalysts is increased, which would affect the adsorption energy and energetic barrier of dissociation of active species for HER.

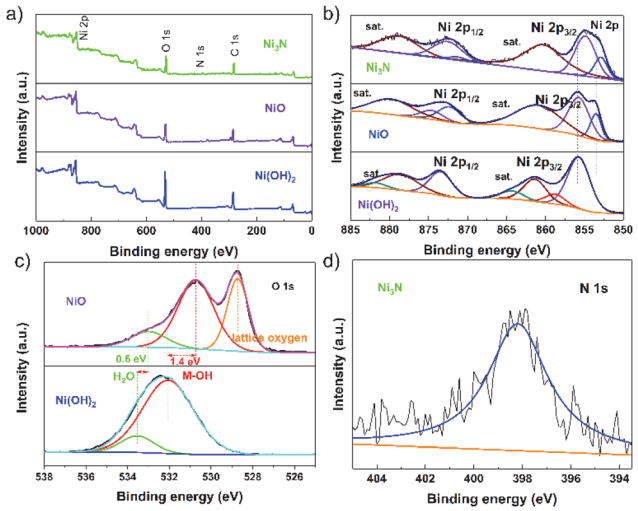

Fig. 2 (a) The XPS survey spectra of Ni_3N, NiO and $Ni(OH)_2$. The high-resolution XPS spectra of (b) Ni and (c) O in the NiO and $Ni(OH)_2$. (d) the XPS spectra of N in Ni_3N.

To assess the electrocatalytic ability to evolve hydrogen, we performed a detailed characterization of electrocatalyst samples with a surface area of 1×1 cm^2. Comparative analyses were carried out to measure the electrocatalytic activities of bare nickel foam (NF), nickel nitride on nickel foam (Ni_3N/NF), nickel oxide on nickel foam (NiO/NF), and nickel hydroxide on nickel foam ($Ni(OH)_2$/NF). The cathodic polarization curves of HER on the electrocatalysts are exhibited in Fig. 3a. The Ni_3N/NF electrocatalyst necessitated an overpotential of merely 135 mV to attain an electrocatalytic current density of 10 mA cm^{-2}. This value is substantially inferior to the overpotentials required by the bare nickel foam (298 mV), nickel oxide/nickel foam (NiO/NF, 177 mV), and nickel hydroxide/nickel foam ($Ni(OH)_2$/NF, 147 mV), highlighting the enhanced efficiency of the Ni_3N/NF catalyst. This indicates that Ni_3N/NF exhibits remarkable catalytic activity towards HER, with a lower onset potential compared to NF, NiO/NF, and $Ni(OH)_2$/NF.

The kinetic parameters of the electrocatalytic reaction were determined by analyzing the polarization curves of the HER, which describe the relationship between overpotential and current density (Fig. 3b). The Tafel slope value of Ni_3N/NF was found to be 96.53 mV dec^{-1}, which is less than that of bare NF (225.03 mV dec^{-1}), $Ni(OH)_2$/NF (128.91 mV dec^{-1}), and NiO/NF (183.91 mV dec^{-1}). This indicates that Ni_3N/NF exhibits a faster kinetic HER process, leading to an improved HER performance.

 This journal is © The Royal Society of Chemistry 2024

Published on 03 1403. Downloaded on 28/11/1404 09:10:16 ..

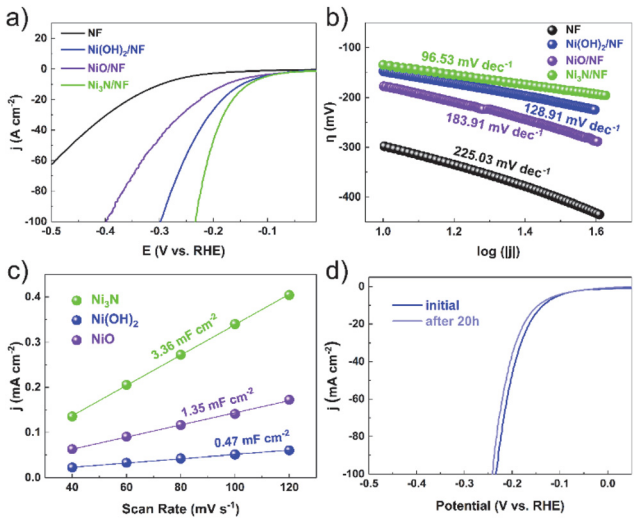

Fig. 3 (a) Polarization curves of Ni_3N, NiO and $Ni(OH)_2$ and Pt/C electrocatalysts. (b) The corresponding Tafel plots of the three catalysts. (c) The C_{dl} calculations of Ni_3N, NiO and $Ni(OH)_2$. (d) Polarization curves of Ni_3N/NF in 1 m KOH before and after 20 h under a certain potential (at −0.15 V *vs.* RHE).

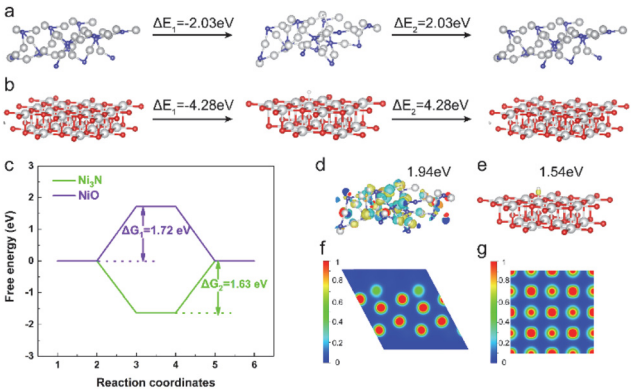

Fig. 4 Schematic slab models of (a) Ni_3N and (b) NiO. (c) Free energy diagram for the HER on three considered models at zero potential. The charge density difference plots for *H on (d) Ni_3N and (e) NiO with an isosurface value of 0.003 e Å^{-3}. Yellow and cyan contours represent electron accumulation and depletion of O-intermediate species, respectively. Electron localization function (ELF) for (f) Ni_3N and (g) NiO.

The electrochemical double-layer capacitance (C_{dl}) is directly proportional to the electrochemical active surface area (ECSA). Consequently, the ECSA was estimated by calculating the C_{dl}. This was achieved by recording cyclic voltammetry curves within a potential window devoid of redox reactions (Fig. S6–S8†). Ni_3N/NF had much larger C_{dl} (3.36 mF cm^{-2}) than $Ni(OH)_2$/NF (0.47 mF cm^{-2}) and NiO/NF (1.35 mF cm^{-2}), showing more electrocatalytic active sites on Ni_3N/NF. Furthermore, electrochemical Impedance spectroscopy (EIS) is utilized to investigate the interfacial characteristics of electrocatalytic materials. As shown in Fig. S9,† the electron-transfer resistance exhibited by Ni_3N/NF is significantly lower compared to that of $Ni(OH)_2$/NF and NiO/NF. This observation is consistent with the outcomes derived from LSV analyses. The long-term stability is an essential parameter for assessing catalyst performance. Before and after testing at the potential of −0.15 V (*vs.* RHE) for 20 h, the polarization curves for Ni_3N/NF exhibit a comparable LSV profile to the initial curve, with an insignificant decrease in current density, as shown in Fig. 3d.

In order to elucidate the intrinsic correlation between the improved electrocatalytic performance and the influence of non-metal elements in catalyzing the hydrogen evolution process (Fig. 4), we conducted calculations to determine the adsorption strength of H atoms on the Ni site in Ni_3N and NiO (Fig. 4a and b). The adsorption strength of H atoms on the Ni site in Ni_3N (*i.e.*, Ni_3N: $\Delta E_{*H} = E_{*H} - E_* = -2.03$ eV) was found to be relatively weaker compared to that of NiO (*i.e.*, NiO: $\Delta E_{*H} = E_{*H} - E_* = -4.28$ eV). However, the desorption energy of H atoms on the Ni site in Ni_3N (*i.e.*, Ni_3N: $\Delta E_{*H} = E_* - E_{*H} = 2.03$ eV) was lower than that of H atoms on the Ni site in NiO (*i.e.*, NiO: $\Delta E_{*H} = E_{*H} - E_* = 4.28$ eV), indicating that H atoms on the Ni site in Ni_3N are more easily desorbed than those on the Ni site in NiO. Furthermore, we have also calculated the Gibbs free energy variation (ΔG) for each fundamental reaction step on the Ni site in Ni_3N and NiO during the HER process (Fig. 4c). The Gibbs free energy difference value of the Ni sites in Ni_3N ($\Delta G_2 = 1.63$ eV) was lower than that of NiO ($\Delta G_1 = 1.72$ eV) during the desorption of hydrogen atoms, suggesting that the catalytic activity of Ni_3N is greater than that of NiO. In order to delve into the intricacies of the doping effect, we conducted an analysis of the charge density difference plots pertaining to *H adsorption. This was done with the objective of qualitatively illustrating the interaction between *H radicals and Ni_3N and NiO. As depicted in Fig. 4d and e, the charge accumulation on the Ni-site radical is more pronounced on Ni_3N (1.94 eV) compared to NiO (1.54 eV), while the charge redistribution for the Ni site on Ni_3N is almost identical to that on NiO.

It is noteworthy that there is a greater transfer of charge from the N atom to the Ni-site in Ni_3N compared to the charge transfer from the N atom to the Ni-site in NiO. Specifically, when Ni_3N interacts with an *H molecule, the Ni-site in Ni_3N exhibits a higher affinity for accepting electrons compared to the Ni-site in NiO, leading to the effective activation of Ni-sites in Ni_3N for the HER. Fig. S10† illustrates that the bandgap of NiO, which is approximately 1.48 eV in the total density of states (TDOS), is larger than that of Ni_3N (which is about 0 eV). Consequently, the conductivity of Ni_3N is higher than that of NiO. Fig. S11† depicts the projected density of states (PDOS) for the d band of Ni in both Ni_3N and NiO. The d-band of the Ni atom in Ni_3N is visibly narrower compared to the d-band of the Ni atom in NiO, indicating the electron localization of the d orbitals of the Ni atom in Ni_3N. The d-band center of the Ni atom in Ni_3N (−2.78 eV) is higher than that of the Ni atom in NiO (−3.42 eV), suggesting that the electron localization function (ELF) identifies the localization of electrons around N atoms on the (001) surface of Ni_3N, while the distribution is

Published on 03 1403. Downloaded on 28/11/1404 09:10:16 ..

uniform within Ni_3N (Fig. 4f). Additionally, the electron distribution around Ni atoms is relatively enhanced, indicating the effective activation of Ni sites. As previously reported, the manipulation of electron localization can be utilized to engineer the energetics of reaction intermediates for electrocatalysis.

Our DFT calculation results display that the improved electrocatalytic performance of Ni_3N primarily stems from the electron-rich interfacial region, which facilitates electron transfer from N-site to Ni-site, leading to charge accumulate on the Ni-site in the Ni_3N and negatively shift the d-band centre of the Ni atom in Ni_3N. Consequently, this promotes the adsorption H_2O to form *H. Moreover, the charge accumulation on the Ni-site radical is more pronounced on Ni_3N compared to NiO for the HER, suggesting the charge transfer for the Ni site on Ni_3N is superior to that on NiO. Our results suggest the notion of orbital-regulated the electronic levels on Ni-site introduces a distinctive methodology for the systematic development of catalysts used for hydrogen evolution in the future.

Conclusions

In conclusion, we have successfully demonstrated the utilization of metallic 3D Ni_3N nanosheets as an exceptional electrode material. Our research presents an innovative yet straightforward approach to enhance the kinetics of water dissociation in Ni_3N, utilizing the electron redistribution in d orbitals induced by oxygen. Compared to the HER activity of NiO, the fabricated Ni_3N demonstrates a higher overpotential, measuring 135 mV when operating at a current density of 10 mA cm^{-2}. XPS analysis indicates that oxygen dopants, possessing a higher electron-pulling capacity, generate additional unoccupied states in the Ni sites. Moreover, DFT calculations elucidate that Ni_3N can also depress the d-band center of Ni sites, thereby catalyzing hydrogen evolution and consequently activating and expediting water dissociation. This innovative concept of electron-regulated electrocatalysis could furnish substantial insights for catalyst design, not only for HER but also for other applications.

Conflicts of interest

There are no conflicts to declare.

Acknowledgements

This work was supported by the fundamental research funds for the Natural Science Foundation of Chongqing (cstc2021jcyj-msxmX0626) and the Science and Technology Research Program of Chongqing Municipal Education Commission (KJZD-K202203201).

References

1 X. Jin, J. Li, Y. Cui, X. Liu, X. Zhang, J. Yao and B. Liu, *Inorg. Chem.*, 2019, **58**, 11630–11635.
2 C. Wei, R. R. Rao, J. Peng, B. Huang, I. E. L. Stephens, M. Risch, Z. J. Xu and Y. Shao-Horn, *Adv. Mater.*, 2019, **31**, e1806296.
3 A. Wu, Y. Xie, H. Ma, C. Tian, Y. Gu, H. Yan, X. Zhang, G. Yang and H. Fu, *Nano Energy*, 2018, **44**, 353–363.
4 P. F. Guo, Y. Yang, B. Zhu, *et al.*, Heterostructural NiFeW disulfideand hydroxide dual-trimetallic core-shell nanosheets for synergistically effective water oxidation, *Carbon Energy*, 2024, e532, DOI: 10.1002/cey2.532.
5 R. R. Chen, G. Chen, X. Ren, J. Ge, S. J. H. Ong, S. Xi, X. Wang and Z. J. Xu, *Angew. Chem., Int. Ed.*, 2021, **60**, 25884–25890.
6 R. R. Chen, Y. Sun, S. J. H. Ong, S. Xi, Y. Du, C. Liu, O. Lev and Z. J. Xu, *Adv. Mater.*, 2020, **32**, e1907976.
7 W. H. Lee, M. H. Han, Y. J. Ko, B. K. Min, K. H. Chae and H. S. Oh, *Nat. Commun.*, 2022, **13**, 605.
8 L. Li, P. Wang, Q. Shao and X. Huang, *Chem. Soc. Rev.*, 2020, **49**, 3072–3106.
9 H. Sun, L. Li, Y. Chen, H. Kim, X. Xu, D. Guan, Z. Hu, L. Zhang, Z. Shao and W. Jung, *Appl. Catal., B*, 2023, **325**, 122388.
10 F. Song, W. Li, J. Yang, G. Han, P. Liao and Y. Sun, *Nat. Commun.*, 2018, **9**, 4531.
11 M. Wang, W. Ma, Z. Lv, D. Liu, K. Jian and J. Dang, *J. Phys. Chem. Lett.*, 2021, **12**, 1581–1587.
12 Y. Yang, Q. Dai, L. Shi, Y. Liu, T. T. Isimjan and X. Yang, *J. Phys. Chem. Lett.*, 2022, **13**, 2107–2116.
13 J. Zhang, Y. Liu, J. Li, X. Jin, Y. Li, Q. Qian, Y. Wang, A. El-Harairy, Z. Li, Y. Zhu, H. Zhang, M. Cheng, S. Zeng and G. Zhang, *ACS Appl. Mater. Interfaces*, 2021, **13**, 3881–3890.
14 Y. Sun, S. Sun, H. Yang, S. Xi, J. Gracia and Z. J. Xu, *Adv. Mater.*, 2020, **32**, e2003297.
15 T. Wu, Y. Sun, X. Ren, J. Wang, J. Song, Y. Pan, Y. Mu, J. Zhang, Q. Cheng, G. Xian, S. Xi, C. Shen, H. J. Gao, A. C. Fisher, M. P. Sherburne, Y. Du, J. W. Ager, J. Gracia, H. Yang, L. Zeng and Z. J. Xu, *Adv. Mater.*, 2023, **35**, e2207041.
16 Y. Yang, P. Li, X. Zheng, W. Sun, S. X. Dou, T. Ma and H. Pan, *Chem. Soc. Rev.*, 2022, **51**, 9620–9693.
17 A. R. Zeradjanin, G. Polymeros, C. Toparli, M. Ledendecker, N. Hodnik, A. Erbe, M. Rohwerder and F. La Mantia, *Phys. Chem. Chem. Phys.*, 2020, **22**, 8768–8780.
18 H. Zhang, J. Wang, F. Qin, H. Liu and C. Wang, *Nano Res.*, 2021, **14**, 3489–3496.
19 S. Chandrasekaran, L. Yao, L. Deng, C. Bowen, Y. Zhang, S. Chen, Z. Lin, F. Peng and P. Zhang, *Chem. Soc. Rev.*, 2019, **48**, 4178–4280.
20 N. Dubouis and A. Grimaud, *Chem. Sci.*, 2019, **10**, 9165–9181.
21 J. Hao, K. Wu, C. Lyu, Y. Yang, H. Wu, J. Liu, N. Liu, W. M. Lau and J. Zheng, *Mater. Horiz.*, 2023, **10**, 2312–2342.
22 H. Jung, S. Choung and J. W. Han, *Nanoscale Adv.*, 2021, **3**, 6797–6826.

 This journal is © The Royal Society of Chemistry 2024

Published on 03 1403. Downloaded on 28/11/1404 09:10:16 ..

23 D. Guan, H. Xu, Q. Zhang, Y.-C. Huang, C. Shi, Y.-C. Chang, X. Xu, J. Tang, Y. Gu, C.-W. Pao, S.-C. Haw, J.-M. Chen, Z. Hu, M. Ni and Z. Shao, *Adv. Mater.*, 2023, **35**, 2305074.
24 X. Li, H. Zhang, X. Li, Q. Hu, C. Deng, X. Jiang, H. Yang and C. He, *Nano Res.*, 2023, **16**, 2245–2251.
25 J. Lu, P.-J. Deng, A. Chen, C. Yang, H. Zhu and H.-P. Liang, *J. Mater. Chem. A*, 2023, **11**, 2452–2459.
26 J. T. Ren, L. Wang, L. Chen, X. L. Song, Q. H. Kong, H. Y. Wang and Z. Y. Yuan, *Small*, 2023, **19**, 2206196.
27 Y. Guo, T. Park, J. W. Yi, J. Henzie, J. Kim, Z. Wang, B. Jiang, Y. Bando, Y. Sugahara, J. Tang and Y. Yamauchi, *Adv. Mater.*, 2019, **31**, 1807134.
28 D. Tian, S. R. Denny, K. Li, H. Wang, S. Kattel and J. G. Chen, *Chem. Soc. Rev.*, 2021, **50**, 12338–12376.
29 C. Yang, K. Shen, R. Zhao, H. Xiang, J. Wu, W. Zhong, Q. Zhang, X. Li and N. Yang, *Adv. Funct. Mater.*, 2022, **32**, 2108167.
30 C. Yang, R. Zhao, H. Xiang, J. Wu, W. Zhong, W. Li, Q. Zhang, N. Yang and X. Li, *Adv. Energy Mater.*, 2020, **10**, 2002260.
31 G.-Q. Yu, B.-Y. Huang, X. Chen, D. Wang, F. Zheng and X.-B. Li, *J. Phys. Chem. C*, 2019, **123**, 21878–21887.
32 Y. Yu, J. Zhou and Z. Sun, *Adv. Funct. Mater.*, 2020, **30**, 2000570.
33 Y. Fang, D. Sun, S. Niu, J. Cai, Y. Zang, Y. Wu, L. Zhu, Y. Xie, Y. Liu, Z. Zhu, A. Mosallanezhad, D. Niu, Z. Lu, J. Shi, X. Liu, D. Rao, G. Wang and Y. Qian, *Sci. China: Chem.*, 2020, **63**, 1563–1569.
34 D. Gao, J. Zhang, T. Wang, W. Xiao, K. Tao, D. Xue and J. Ding, *J. Mater. Chem. A*, 2016, **4**, 17363–17369.
35 X. Gao, X. Liu, W. Zang, H. Dong, Y. Pang, Z. Kou, P. Wang, Z. Pan, S. Wei, S. Mu and J. Wang, *Nano Energy*, 2020, **78**, 105355.
36 X. Gao, W. Zang, X. Li, Z. Wang, L. Zheng and Z. Kou, *Chem. Eng. J.*, 2023, **451**, 138698.
37 M. Li, X. Wu, K. Liu, Y. Zhang, X. Jiang, D. Sun, Y. Tang, K. Huang and G. Fu, *J. Energy Chem.*, 2022, **69**, 506–515.
38 S. Niu, Y. Fang, J. Zhou, J. Cai, Y. Zang, Y. Wu, J. Ye, Y. Xie, Y. Liu, X. Zheng, W. Qu, X. Liu, G. Wang and Y. Qian, *J. Mater. Chem. A*, 2019, **7**, 10924–10929.
39 B. Zhang, J. Wang, J. Liu, L. Zhang, H. Wan, L. Miao and J. Jiang, *ACS Catal.*, 2019, **9**, 9332–9338.
40 D. Zhang, H. Li, A. Riaz, A. Sharma, W. Liang, Y. Wang, H. Chen, K. Vora, D. Yan, Z. Su, A. Tricoli, C. Zhao, F. J. Beck, K. Reuter, K. Catchpole and S. Karuturi, *Energy Environ. Sci.*, 2022, **15**, 185–195.
41 P. Zhou, G. Zhai, X. Lv, Y. Liu, Z. Wang, P. Wang, Z. Zheng, H. Cheng, Y. Dai and B. Huang, *Appl. Catal., B*, 2021, **283**, 119590.
42 X. Jin, J. Li, Y. Cui, X. Liu, K. Wang, Y. Zhou, W. Yang, X. Zhang, C. Zhang, X. Jiang and B. Liu, *Int. J. Hydrogen Energy*, 2019, **44**, 5739–5747.
43 D. Shah, S. Bahr, P. Dietrich, M. Meyer, A. Thißen and M. R. Linford, *Surf. Sci. Spectra*, 2019, **26**, 014023.